AGU PUBLICATIONS

JGR

Journal of Geophysical Research: Space Physics

RESEARCH ARTICLE

10.1002/2016JA022694

Special Section:
Energetic Electron Loss and its Impacts on the Atmosphere

Dependence of EMIC wave parameters during quiet, geomagnetic storm, and geomagnetic storm phase times

A. J. Halford[1,2], B. J. Fraser[3], S. K. Morley[4], S. R. Elkington[5], and A. A. Chan[6]

[1]Department of Physics and Astronomy, Dartmouth College, Hanover, New Hampshire, USA, [2]NASA Goddard Space Flight Center, Greenbelt, Maryland, USA, [3]Centre for Space Physics, University of Newcastle, Callaghan, New South Wales, Australia, [4]Space Science and Applications (ISR-1), Los Alamos National Laboratory, Los Alamos, New Mexico, USA, [5]LASP, University of Colorado Boulder, Boulder, Colorado, USA, [6]Department of Physics and Astronomy, Rice University, Houston, Texas, USA

Key Points:
- The occurrence of EMIC waves is not well described by a single geomagnetic index
- EMIC wave occurrence is highly dependent upon geomagnetic storm phase
- The local plasma conditions when there is EMIC wave activity differ significantly from those when no EMIC waves are seen

Supporting Information:
- Supporting Information S1

Correspondence to:
A. J. Halford,
alexa.halford@gmail.com

Citation:
Halford, A. J., B. J. Fraser, S. K. Morley, S. R. Elkington, and A. A. Chan (2016), Dependence of EMIC wave parameters during quiet, geomagnetic storm, and geomagnetic storm phase times, *J. Geophys. Res. Space Physics*, *121*, 6277–6291, doi:10.1002/2016JA022694.

Received 11 MAR 2016
Accepted 3 JUN 2016
Accepted article online 8 JUN 2016
Published online 9 JUL 2016

Abstract As electromagnetic ion cyclotron (EMIC) waves may play an important role in radiation belt dynamics, there has been a push to better include them into global simulations. How to best include EMIC wave effects is still an open question. Recently many studies have attempted to parameterize EMIC waves and their characteristics by geomagnetic indices. However, this does not fully take into account important physics related to the phase of a geomagnetic storm. In this paper we first consider how EMIC wave occurrence varies with the phase of a geomagnetic storm and the *SYM-H*, *AE*, and *Kp* indices. We show that the storm phase plays an important role in the occurrence probability of EMIC waves. The occurrence rates for a given value of a geomagnetic index change based on the geomagnetic condition. In this study we also describe the typical plasma and wave parameters observed in *L* and magnetic local time for quiet, storm, and storm phase. These results are given in a tabular format in the supporting information so that more accurate statistics of EMIC wave parameters can be incorporated into modeling efforts.

1. Introduction

Electromagnetic ion cyclotron (EMIC) waves and their relationship with geomagnetic storms [e.g., *Halford et al.*, 2010; *Usanova et al.*, 2012; *Halford et al.*, 2015] have been an area of great interest as they are believed to potentially be an important loss mechanism for radiation belt electrons [e.g., *Engebretson et al.*, 2008; *Blum et al.*, 2009; *Fraser et al.*, 2010]. EMIC waves are identified as transverse and left-hand polarized and are regularly observed at middle to high latitudes on the ground (approximately > 50). Ground-based studies typically classify EMIC waves within the Pc1–Pc2 band (0.1–5 Hz). In space, the frequency of EMIC waves is determined by the ion gyrofrequencies in the source region, typically also found in the 0.1–5 Hz range inside the magnetosphere. They are generated by temperature anisotropies often produced during enhancements of ring current protons (10–100 keV) or set up by magnetopause compressions, both of which provide free energy for wave growth [e.g., *Cornwall*, 1965; *Olson and Lee*, 1983]. During storms, the instability threshold can be reduced when the ring current encroaches on the cold plasma population in the plasmasphere and in plasmaspheric plumes [e.g., *Criswell*, 1969; *Spasojevic et al.*, 2003; *Fraser et al.*, 2005; *Kotova*, 2007]. However, overlap between the ring current and plasmasphere is not a necessary nor sufficient condition for wave growth [e.g., *Halford et al.*, 2015; *Denton et al.*, 2015]. The preferred region of wave growth for EMIC waves is in regions of minimum *B* where the wave vector is parallel to the magnetic field, often found at the equator [*Gomberoff and Neira*, 1983; *Kozyra et al.*, 1984; *Fraser et al.*, 1992; *Gary et al.*, 1994]. Minimum *B* regions can also be found in the outer dayside magnetosphere, near the magnetopause where the minimum *B* surface bifurcates leading to Shabansky orbits [e.g., *McCollough et al.*, 2010; *Liu et al.*, 2012; *McCollough et al.*, 2012; *Liu et al.*, 2013; *Allen et al.*, 2015]. An important part of understanding the theory and generation mechanism of EMIC waves and their relationship with geomagnetic storms, the ring current, and the radiation belts is to know where, when, and under what magnetospheric and plasma conditions EMIC waves are observed.

As the bounce-averaged pitch angle diffusion of MeV electrons with EMIC waves can easily stay near or above the local strong diffusion limit in the outer regions of the radiation belts [*Summers et al.*, 2007a], EMIC waves are thought to potentially be an important player in radiation belt dynamics. However, this has to be balanced with the fact that EMIC waves are relatively localized and their occurrence rates peak at higher *L* values

[e.g., *Anderson et al.*, 1992a; *Halford et al.*, 2010; *Min et al.*, 2012; *Usanova et al.*, 2013; *Allen et al.*, 2015; *Saikin et al.*, 2015] where there are fewer radiation belt electrons to interact with. Their relative importance, when compared with loss mechanisms that are slower, but last longer and cover larger regions of the radiation belts, is still debated. Thus, many previous studies have considered these effects on radiation belts; some with statistical approaches [e.g., *Meredith et al.*, 2003; *Usanova et al.*, 2014], modeling [e.g., *Jordanova*, 2007; *Denton et al.*, 2015], case studies, and proxies for EMIC wave activity [*Sandanger et al.*, 2009; *Spasojevic and Fuselier*, 2009; *Blum et al.*, 2009]. Whether the waves affect radiation belt dynamics depends in part on where and when they occur as well as the local plasma conditions in the region.

Although EMIC waves can be modeled in a localized sense [e.g., *Denton et al.*, 2014, 2015; *Kim and Johnson*, 2016], it is currently difficult to include them in large global MHD models. Global models can include the effects of EMIC waves by using the ion temperature anisotropy of ion species generated as a proxy for EMIC waves [e.g., *McCollough et al.*, 2010]. EMIC waves can also be included though empirical statistical results from satellite missions such as CRRES [e.g., *Shprits et al.*, 2007; *Ni et al.*, 2009; *Shprits et al.*, 2013]. The question then arises, what is the best way to create such an empirical model?

There are different methods by which models can include the effects of EMIC waves on radiation belt dynamics. EMIC waves, as with other magnetospheric phenomena, are often parameterized by geomagnetic indices [e.g., *Gannon et al.*, 2007; *Usanova et al.*, 2012; *Keika*, 2013; *Horne et al.*, 2013; *Meredith et al.*, 2014]. Others have used the phases of geomagnetic storms [*Ilie et al.*, 2008; *Halford et al.*, 2010, 2015; *Murphy et al.*, 2015; *Katus et al.*, 2015]. It is important to understand which method will best capture the physics associated with EMIC waves. Future work should also consider not just the proxies which describe the physics associated with EMIC wave observations but EMIC wave-particle dynamics. In this current paper we will first look at how EMIC wave occurrence relates to geomagnetic indices as well as storm phase. As it becomes clear that there is a strong storm phase dependance, we will consider the typical parameters for EMIC waves during the CRRES mission under different geomagnetic conditions. This study is a first step at identifying a typical EMIC wave in the inner magnetosphere in the region of the outer radiation belt using the CRRES data set. When comparing the results from this paper to the typical waves observed for other satellite missions, it is important to remember that CRRES was operational during a very active solar cycle compared to the solar cycles that have followed [see, e.g., *Morley et al.*, 2016, Figure 1].

2. Data Analysis and Methodology

2.1. The CRRES Mission

The CRRES mission was the predecessor to the Van Allen Probes with a very similar orbit and set of instrumentation. The CRRES mission, however, did not fully precess around the Earth but swept from an apogee of 08:00 LT at the time of launch from July 1990 through midnight at a rate of 1.3 h per month to approximately 14:00 magnetic local time (MLT) when the CRRES mission concluded in October 1991 [*Fraser and Nguyen*, 2001]. The orbital period was approximately 10 h with an apogee of 6.3 R_E, a perigee of 350 km, and an inclination of 18.3° [*Fraser and Nguyen*, 2001]. This allowed CRRES to cover geomagnetic latitudes between ±30° and view McIlwain L shells up to approximately 8 [*McIlwain*, 1966]. The satellite instrumentation included an Air Force Geophysics Laboratory (AFGL) fluxgate magnetometer [*Singer et al.*, 1992] and the Iowa plasma wave experiment [*Anderson et al.*, 1992b].

The three component fluxgate magnetic field data were sampled at 16 Hz. The *X*, *Y*, and *Z* sensor signals were sampled by a 12 bit A/D converter at 16 times/1.024 s. CRRES was in its high sensitivity mode for ~75% of its orbit, out beyond $\approx 3R_E$ [*Singer et al.*, 1992]. Inside of $L \approx 3$ EMIC waves were unable to be identified.

The University of Iowa/AFGL plasma wave instrument provided the cold electron number density data [*Anderson et al.*, 1992b] via the intense upper hybrid resonance frequency, f_{uhr}, as described in *Halford et al.* [2015].

The CRRES software used the Olson and Pfitzer static analytical model of the Earth's magnetic field [*Olson and Pfitzer*, 1974] to calculate the ephemeris parameters. As consistent upstream monitoring of the solar wind was not available during the CRRES mission, the inputs necessary to run the more modern dynamic Tsyganenko models were not available [e.g., *Tsyganenko and Sitnov*, 2005]. Thus, the static Olsen-Pfitzer model, which has been shown to provide a good representation of the external magnetic field in the inner magnetosphere [see, e.g., *Friedel et al.*, 2005; *Morley et al.*, 2013], was used. The internal field model ($R < 2$) is represented by a fixed dipole, and the external field model takes into account quiet time magnetosphere conditions

including contributions from the magnetopause, tail, and ring currents and is valid within 15 R_E of the Earth [*Olson and Pfitzer*, 1974]. This modeling mapped the orbit of CRRES to McIlwain *L* values up to approximately 8 [*McIlwain*, 1966].

2.2. Magnetospheric Condition

During the CRRES mission 124 storms were identified using the Kyoto *SYM-H* index [*Halford et al.*, 2010] and a plot of each of the storms and their phases can be found in *Halford* [2012, Figure 5.5]. Each geomagnetic storm is divided into three phases, preonset, main, and recovery as described in *Halford et al.* [2010] and *Halford et al.* [2015]. As each storm has phases of varying lengths, each phase has been defined based on characteristics of the *SYM-H* index, which is a higher temporal and spatial version of the 1 h *Dst*. We have used the *SYM-H* index to define our storms and the phases as it is a proxy for the strength of the ring current, perhaps a primary driver of EMIC waves during geomagnetic storms. Magnetospheric compressions, which are another driver of EMIC waves [e.g., *Anderson et al.*, 1992a; A.J. Halford and I. R. Mann, Solar Wind Compression Generation of Coincident EMIC and Whistler Mode Chorus and Hiss Waves, submitted to *Journal of Geophysical Research*, 2016], are also well captured by the *SYM-H* index [see *Carter et al.*, 2015]. The preonset phase is defined as the 3 h prior to the onset of a storm. The main phase is taken as the onset to the minimum *SYM-H* value is reached (mean length of ~9 h). In this study the recovery phase definition is from the end of the main phase until *SYM-H* has recovered 80% of the minimum value reached during the storm or until the onset of the next storm (mean length of ~18 h). A geomagnetic storm is defined when any of the three phases is occurring and quiet conditions as when a storm is not in progress. These definitions allow for up to 3 h of overlap between the recovery phase and preonset of the following storm.

2.3. EMIC Waves

This study uses the same set of EMIC waves as was used in *Halford et al.* [2015], which is an updated list from that used in *Halford et al.* [2010]. The magnetometer data were processed and studied for 8 h centered on apogee at *L* values for $L \geq 3$. Since the equatorial ring current is typically geo-effective at $L > 3$, it is considered that very few EMIC waves observed on lower *L* values would potentially be generated by the storm time dynamics. We note that *Kasahara et al.* [1992] reported EMIC at $L < 3$, using the Akebono satellite, though occurrence rates were not presented. As the regions where Akebono and CRRES were able to measure EMIC waves do not overlap we leave further discussion of EMIC at low *L* to future work. The waves were identified visually using CRRES data processed by T.S. Nguyen between 0 and 4 Hz [*Fraser and Nguyen*, 2001] although the bandwidth covered frequencies from 0 to 8 Hz. No EMIC waves were found in the data set above 4 Hz. A total of 913 EMIC wave events (5970 min) were identified throughout the CRRES mission. There were 492 (totaling 3407 min) EMIC wave events observed during geomagnetic storms. Although the recovery phase of the storm was the longest of the three phases, the main phase saw the largest amount of wave activity at 275 events totaling 1907 min. The recovery phase had 189 individual events for 1356 min of wave activity. The preonset phase saw the fewest with 34 individual events for 195 min of wave activity. This is possibly due to the CRRES orbit not fully traversing the noon sector where compression driven waves are expected to have a peak occurrence. There are 51 min of wave activity overlap with the recovery phase of the previous storm. For these events the relevant parameters are counted once as storm time and then counted in each subset that they occurred in, preonset and recovery phase.

3. *AE*, *SYM-H*, *Kp*, or Storm Phase?

Each of the commonly used indices, *AE*, *SYM-H*, and *Kp*, has been used to try to quantify wave-particle effects on the radiation belts [e.g., *Kasahara et al.*, 1992; *Li et al.*, 2009; *Usanova et al.*, 2012; *Meredith et al.*, 2014]. However, each of these indices has their own pitfalls. For instance, the *SYM-H* index is an ideal candidate for EMIC wave studies as we typically think of the *SYM-H* or *Dst* indices as a measure of the strength of the ring current [e.g., *Dessler and Parker*, 1959; *Sckopke*, 1966; *Sugiura*, 1964], one region which can provide free energy for the growth of EMIC waves. However, the *SYM-H* and *Dst* indices can be greatly affected by other current systems as well as ground induced currents [e.g., *Siscoe and Crooker*, 1974; *Carter et al.*, 2015, and references within]. The results from *Halford et al.* [2010] imply that a particular *SYM-H* value during the main phase may not have the same local plasma conditions, e.g., the same temperature anisotropy and thus correlation to EMIC waves, during the recovery phase of the storm.

By contrast, the *AE* and *Kp* indices are often thought of as indicators of substorm activity [e.g., *Rostoker*, 1972; *Kamide and Akasofu*, 1983] and enhanced magnetospheric convection [e.g., *Thomsen*, 2004], respectively.

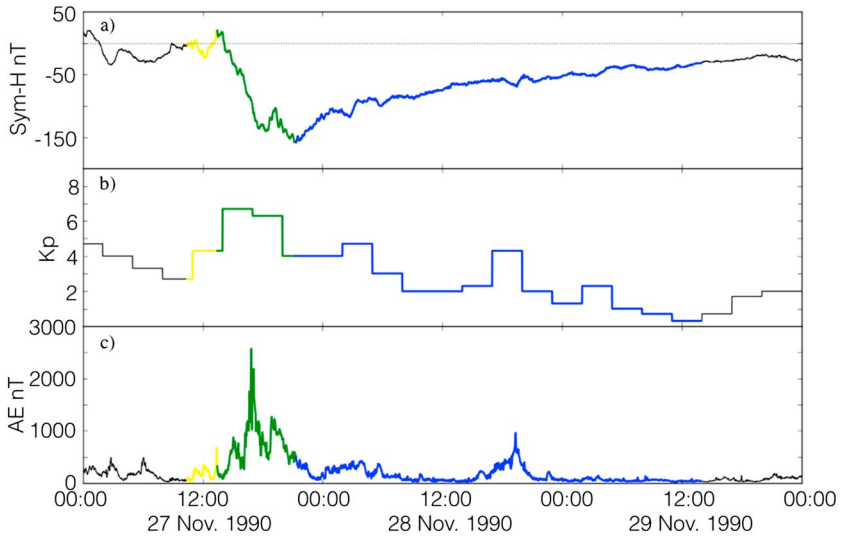

Figure 1. An example storm during the CRRES mission from 27 November to 29 November 1990. (a) The *SYM-H* index, (b) the *Kp* index, and (c) the *AE* index; the onset is highlighted in yellow, the main phase in green, and the recovery phase in blue.

It is important to ask the question: how would these processes effect the generation of EMIC waves? Substorm activity may provide enough free energy into the ring current through proton substorm injections, as suggested by the results shown in *Blum et al.* [2015] and previously posed in other work [e.g., *Bossen et al.*, 1976; *Kangas et al.*, 1998; *Fraser et al.*, 2012]. In general, *Kp* and *SYM-H* follow each other [e.g., *Saba et al.*, 1997]. If there is a relationship with EMIC waves and the *SYM-H* index, perhaps there is one with *Kp*. *Kp* is also often thought to describe convection of the magnetosphere and thus the evolution of the plasmasphere. As EMIC waves have been thought to have an important relationship with the plasmasphere and plasmaspheric plumes, perhaps the *Kp* index would work well as a proxy for EMIC wave occurrences as suggested by *Kasahara et al.* [1992] for EMIC at $L < 3$.

During both geomagnetic storms and quiet conditions, as defined by the *SYM-H* index discussed above, one can find a large range of *AE* and *Kp* values. The storm on 27 November 1990, shown in Figure 1, provides an example where the same values of *AE* and *Kp* can be found during quiet, preonset, main, and recovery phases. If EMIC waves are correlated to geomagnetic processes related to *AE* or *Kp* instead of *SYM-H* or storm phase, we may expect similar occurrence probabilities of observing EMIC waves for a given index value regardless of geomagnetic condition. As many empirical models use the *AE* or *Kp* indices to describe wave activity, it is important to know if this is valid or if storm phase plays perhaps a greater role. In order to determine if either storm phases or indices have a greater role, we have calculated the occurrence probability of EMIC waves for a given *SYM-H* (Figure 2), *AE* (Figure 3), and *Kp* (Figure 4) value for all EMIC waves, those observed during quiet geomagnetic conditions, and those found during geomagnetic storms and their phases.

In order to address how often a given value of an index is observed by storm phase, we have sorted *SYM-H*, *AE*, and *Kp* values by geomagnetic condition as defined in section 2.2. These results can be seen in Figures 2–4 where the occurrence percentage for the *SYM-H*, *AE*, and *Kp* indices, respectively, during the CRRES mission are shown in the yellow bars for each bin. The occurrence distribution for the indices differs between each defined geomagnetic condition. For comparison the percentage of EMIC waves observed in a given bin is plotted with the blue bars. As can be seen, the occurrence distribution of EMIC waves does not consistently follow the distribution of the indices for a given geomagnetic condition. This tells us that the occurrence of EMIC waves is not the same for a given index value, and thus, the indices are not a good proxy for EMIC wave activity.

We have calculated the occurrence rate of EMIC waves for a given index bin (the blue lines) during a given geomagnetic condition (the number of minutes of EMIC wave activity in a given bin divided by the number of minutes of satellite dwell time in that bin). For example, in Figure 2 the occurrence of EMIC waves in the −50 to −40 nT *SYM-H* bin for all EMIC waves as well as during quiet conditions is 1.5% and during storm conditions is 1.6%. However, there are much larger differences for this bin if we consider the individual phases. During

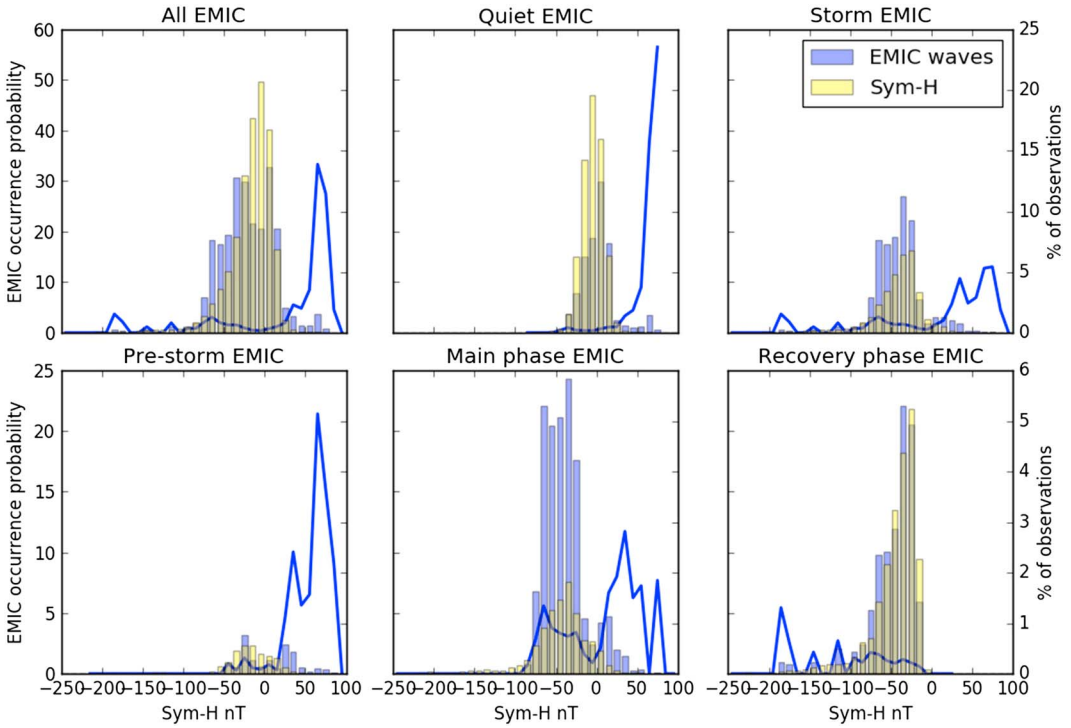

Figure 2. The blue lines represent the occurrence probability of EMIC waves for a given *SYM-H* value for all times, quiet and storm periods, and during the prestorm, main phase, and recovery phases. The blue bar graphs show the percent of EMIC waves observed in a given bin and the yellow bar graphs show the percent of *SYM-H* observations in a given bin.

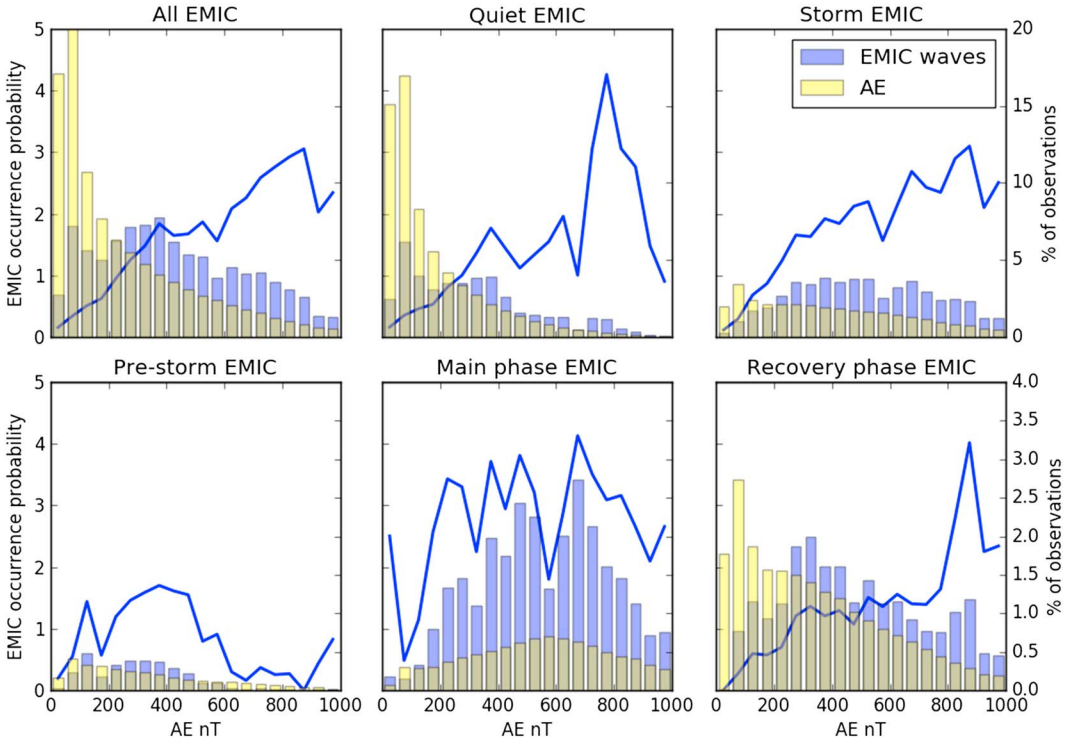

Figure 3. The blue lines represent the occurrence probability of EMIC waves for a given *AE* value for all times, quiet and storm periods, and during the prestorm, main phase, and recovery phases. The blue bar graphs show the percent of EMIC waves observed in a given bin and the yellow bar graphs show the percent of *AE* observations in a given bin.

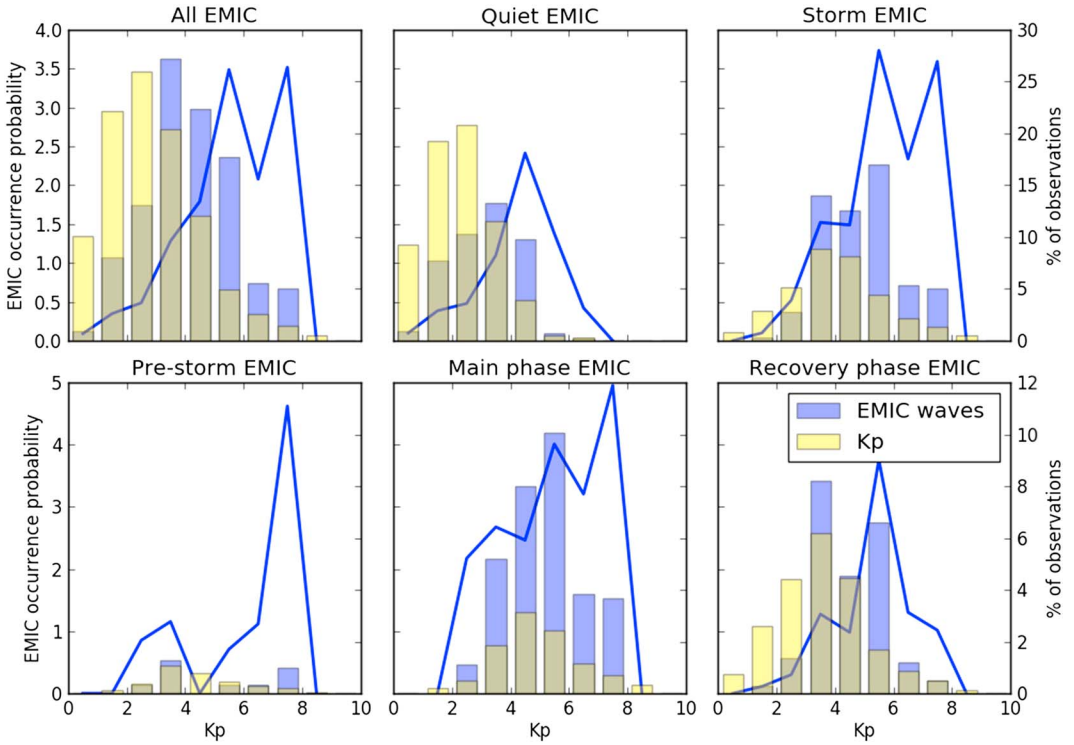

Figure 4. The blue lines represent the occurrence probability of EMIC waves for a given *Kp* value for all times, quiet and storm periods, and during the prestorm, main phase, and recovery phases. The blue bar graphs show the percent of EMIC waves observed in a given bin and the yellow bar graphs show the percent of *Kp* observations in a given bin.

the main phase when most radiation belt loss is observed, the occurrence rate is approximately 3.3% where as during the preonset and recovery phase, when the radiation belts are often observed to recover, it is ~0.8%.

For the *SYM-H* index, as shown in Figure 2, the highest occurrence probabilities are found when *SYM-H* is positive and thus during geomagnetic compressions. This agrees well with previous observations where the highest occurrences of EMIC waves found in the noon sector and at higher *L* values likely due to sudden impulse events [e.g., *Anderson et al.*, 1992a; *Usanova et al.*, 2012]. This is followed by the main phase where the occurrences are generally elevated when compared to the recovery phase or even storm time when taken as a whole. Again, as EMIC waves are expected to grow from an enhancement of the ring current, this result is expected. However, it may not be as expected to find the discrepancy between the same *SYM-H* bins during both the main and recovery phases as it is assumed that the ring current would be equally "enhanced" regardless of the storm phase. The free energy necessary to grow EMIC waves is not solely provided by an enhancement of the ring current but specifically by a temperature anisotropy in the ion populations. The temperature anisotropy inside of the ring current specifically, and more generally throughout the magnetosphere, likely evolves throughout a geomagnetic storm. Perhaps it is this change in temperature anisotropy and available free energy and thus EMIC wave occurrence, which is better captured by considering storm phase than the specific value of an index.

Another thing to note with the discrepancy between the main phase and recovery phase statistics is when one looks at the lowest *SYM-H* values (<−100 nT). The occurrence rate during the main phase drops off to nearly zero, while the recovery phase stays slightly elevated. This may be due to an increase in the amount of oxygen in the ring current during the main phase due to ionospheric outflow [e.g., *Glocer et al.*, 2009]. Increased amounts of oxygen can damp the wave growth of EMIC waves in the helium and hydrogen bands [e.g., *Omidi et al.*, 2013]. Oxygen also has a much shorter lifetime in the ring current than the lighter ions meaning that within the first few hours of the recovery phase at higher *L* values [e.g., *Gerrard et al.*, 2014], when they *SYM-H* index is still disturbed and there may still be temperature anisotropies within the helium and hydrogen ion populations, EMIC waves may be able to once again grow.

The relationship between substorms (or *AE*) and EMIC waves has long been proposed [e.g., *Ishida et al.*, 1987; *Kangas et al.*, 1998; *Wanliss and Showalter*, 2006] and some observational evidence is found [e.g., *Kangas et al.*, 1998; *Blum et al.*, 2015]. Again the free energy to grow the wave potentially comes from the particle injections related to the substorm. When we consider the occurrence frequency of EMIC waves with respect to *AE*, Figure 3 (top left), we see a fairly steady rise as *AE* increases. This trend is observed during quiet and recovery conditions, however, there is an increase at the lower *AE* values during the preonset phase. Although the occurrence rates found during the main phase are a bit scattered, they appear to be elevated regardless of the *AE* index itself. This lack of a strong correlation during both the prestorm and main phase is likely due to the driver during these different conditions. Neither the compressions expected in the preonset phase nor the storm time ring current enhancements are well described by the *AE* index. We note in this context that due to the sparse solar wind monitoring for the CRRES era that we cannot explicitly study the link between compressions and EMIC with this data set. During quiet and recovery phase conditions, substorm proton injections may become an important source of free energy to grow EMIC waves leading to the higher occurrence rates at large *AE* values during these geomagnetic conditions. However, like the *SYM-H* index, the storm phase has a more predictive power for the occurrence of EMIC waves than for a given *AE* index value.

As many global models which include empirical occurrences of waves use the *Kp* index, it has been included here and shown in Figure 4. The occurrence probability of EMIC waves during quiet (nonstorm) conditions has a peak at $Kp = 4–5$. Above $Kp = 5$ it is likely that we have entered into the main phase of a geomagnetic storm. Thus, it is likely, although not shown here, that this population is, at least in part, due to geomagnetic compressions that continue through the early main phase. During all three phases of a geomagnetic storm the probability of seeing an EMIC wave goes up with *Kp*; however, the distribution is much broader during the main phase, as seen with the other two indices and once again the storm phase and geomagnetic condition appear to play an important role in whether or not one expects EMIC waves.

Regardless of the index used, storm phase has a significant effect on the expected occurrence of EMIC waves. This is likely due to the physical processes observed during different geomagnetic conditions. Specifically, the availability of free energy though a local increase in the ion temperature anisotropy necessary to grow EMIC waves can differ greatly between storm phases. We will now consider the typical (median) characteristics of EMIC waves by L and MLT.

4. Occurrence of EMIC Waves

To help us understand where EMIC waves occur, and how this changes with magnetospheric conditions, Figure 5 presents a series of polar plots of the EMIC wave occurrence rates. Figure 5 (top row) shows quiet time and storm time data; Figure 5 (bottom row) shows the occurrence rates in each of the storm phases. We consider bins of 0.5 *L* and 1 h in MLT to gather occurrence rate information, similar to the techniques used by *Usanova et al.* [2012]. The longest time periods used in our work are 60 s resolution, and thus, the bin is considered statistically valid if there are at least 40 min of CRRES dwell time spent in the bin. If the bin has less than 40 min of dwell time, we exclude the bin due to insufficient sampling. Most bins which had data collected during the CRRES mission were found to satisfy this criteria for $L < 7.5$ and in the dusk sector. The smaller polar plots embedded in Figure 5 have the bin filled yellow if there was enough time to be statistically valid and blue if not for a given magnetospheric condition. Tables of the occurrence percentage and satellite dwell time are provided in the supporting information.

The normalized occurrence rates for bins where EMIC waves were observed during different magnetospheric conditions can be seen in Figure 5. Although the occurrence rates appear to be low in both quiet and storm time, the occurrence rates are clearly larger during geomagnetic storms. During quiet geomagnetic storm conditions the maximum occurrence rates were found to be ~11% with a minimum of <0.1% compared to the maximum found during storm times of ~14.5% and a minimum of ~0.2%. The storm time means are greatly affected by both the main and recovery phase statistics which differ significantly from each other.

Although the preonset phase does not contain many bins which have enough dwell time to be valid as well as few EMIC wave occurrences, the occurrence rates increase around the dayside, where the majority of EMIC waves are known to occur (Figure 5) [e.g., *Anderson et al.*, 1992a; *Usanova et al.*, 2012]. It is also found that these rates are typically higher than those found during the recovery phase of the geomagnetic storm with a maximum of ~13.6% and a mean of ~6.3%, but not as large as those found to occur during the main phase. Though there is some overlap between these periods and the late recovery phase, the reported rates do not

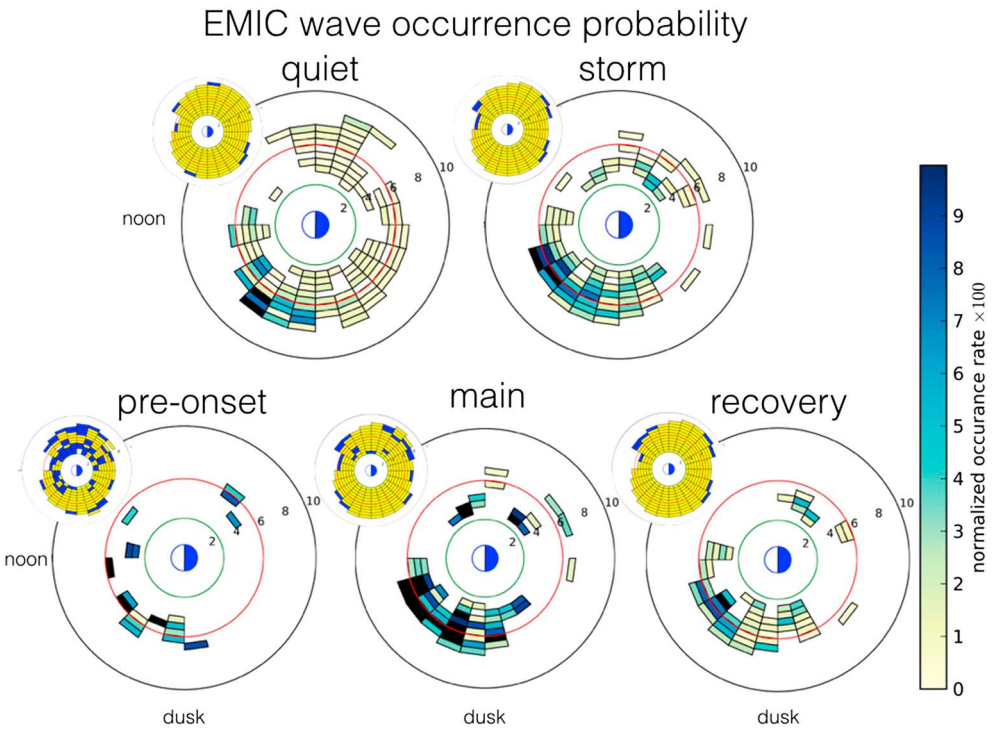

Figure 5. Polar plots of the EMIC wave occurrence rates during quiet, storm, preonset, main, and recovery phases. The inlaid polar plots show yellow when a bin has enough satellite dwell time to be valid and blue when there is not enough dwell time, and white when it was not sampled. The green circle is at $L = 3$, the red at $L = 6$, and black at $L = 9$.

change significantly when overlapping phases are removed from this analysis. With the CRRES mission ending prior to traversing around the noon sector, a location where likely many EMIC waves are caused by dynamics associated with magnetospheric compression, we will require new sources of data to confirm this trend.

The main phase is found to be where the highest occurrence rates occur with a maximum of ~34% and a minimum occurrence rate of ~0.7%. In general, the mean occurrence rate for EMIC waves during the main phase is ~10%. As seen in Figure 5, the occurrence rates tend to increase at higher L and as one moves around the dusk sector toward noon. During the CRRES mission the main phase was where the majority of EMIC waves were found to occur [*Halford et al.*, 2010], and this holds true once the event occurrences have been normalized to the spacecraft dwell time.

The recovery phase has the lowest occurrence rates observed during geomagnetic storms with a maximum of ~10.8% and a minimum of ~0.3%. These values are more closely related to the quiet time levels than those found during the other two storm phases. The recovery phase shows the same trend as the other magnetospheric conditions in that as one moves to higher L and around to noon, there is a slight increase in the observed rates.

5. Cold Plasma Density and EMIC Waves

The median number density of the cold electrons as determined by the upper hybrid frequency is shown for the different magnetospheric conditions in Figure 6 for all the EMIC waves observed during the CRRES mission and during the different phases of a geomagnetic storm. The inset plots in Figure 6 show the median density for each bin during a given magnetospheric condition when no EMIC waves were observed. This becomes a baseline that can be used to compare how the density may differ during EMIC wave activity as done in *Halford et al.* [2015]. On average, the density was observed to be higher during the times when EMIC waves were observed. The median as well as the upper and lower quartiles for the cold plasma number density during EMIC waves is provided in the supporting information.

The median cold plasma number density for EMIC waves during geomagnetic storms was 36 cm^{-3} and the main phase saw the highest median densities at 45 cm^{-3} as seen in Figure 6. A more interesting statistic is

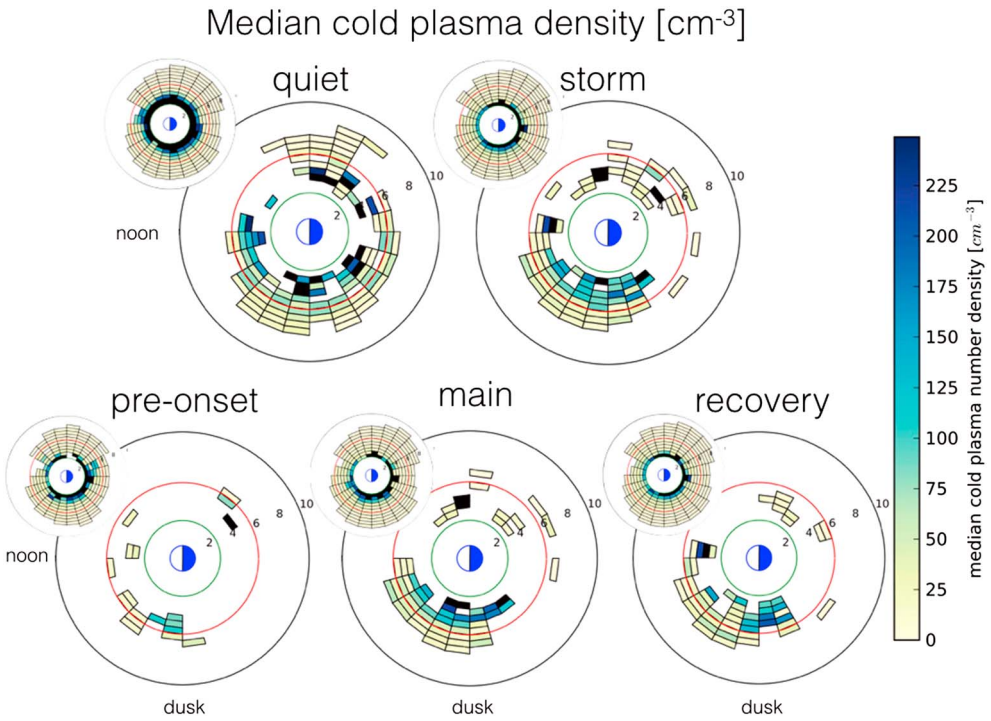

Figure 6. Polar plots of the median cold plasma density during quiet, storm, preonset, main, and recovery phases. The inlaid polar plots show the median cold plasma number density when there were no EMIC waves observed for a given geomagnetic condition. The green circle is at $L = 3$, the red at $L = 6$, and black at $L = 9$.

to look at how the median densities during EMIC waves compare to when EMIC waves were not observed [*Halford et al.*, 2015]. On average the cold plasma densities observed during EMIC waves were approximately 3 times larger than those observed when no EMIC waves were present, with no dependence on geomagnetic index or storm phase. It is important to point out that this does not necessarily mean that EMIC waves occurred in plasmaspheric plumes or the plasmasphere, as this increased density may still be small when compared to plume/plasmasphere densities.

6. The Local α^* Parameter and EMIC Waves

As EMIC waves are thought to potentially be an important contribution to trapped particle loss, especially during the main phase, for radiation belt electrons, we can consider the α^* parameter which in part determines the rate that EMIC waves pitch angle scatter electrons into the atmosphere [e.g., *Summers and Thorne*, 2003]. The values for the parameters in the dispersion relation, as well as α^*, change under different magnetospheric conditions. The parameter α^* is defined as

$$\alpha^* = \frac{\Omega_e^2}{\omega_{pe}^2} = \frac{V_A^2}{\epsilon c^2} = \frac{B_o^2}{4\pi N_o}\frac{1}{m_e c^2}, \tag{1}$$

where $\epsilon = m_e/m_p$. Thus, α^* can be thought of as proportional to the Alfven velocity squared, V_A^2, or the magnetic energy per a particle $\frac{B_o^2}{4\pi N_o}$ [e.g., *Summers et al.*, 2007b], where B_o and N_o are the background magnetic field and cold plasma density, respectively. The effect of the duskside plasmaspheric bulge can be seen in the decrease of the α^* values on the duskside of the magnetosphere.

The local α^* parameter during EMIC waves (Figure 7) are significantly lower (~0.5) from the α^* observed when EMIC waves are not observed (inlayed plots in Figure 7). This is expected as α^* is proportional to the magnetic field and inversely proportional to the cold plasma density. As shown in section 5, the density is observed to be higher when EMIC waves occur, thus lowering α^*. On average the α^* values observed during quiet geomagnetic conditions (median $\alpha^* = 0.009$) are lower than those found during geomagnetic storms (median $\alpha^* = 0.011$). However, the lowest values are observed during the main phase of geomagnetic storms where the median $\alpha^* = 0.008$. The preonset and recovery phases both see higher values on average and are more

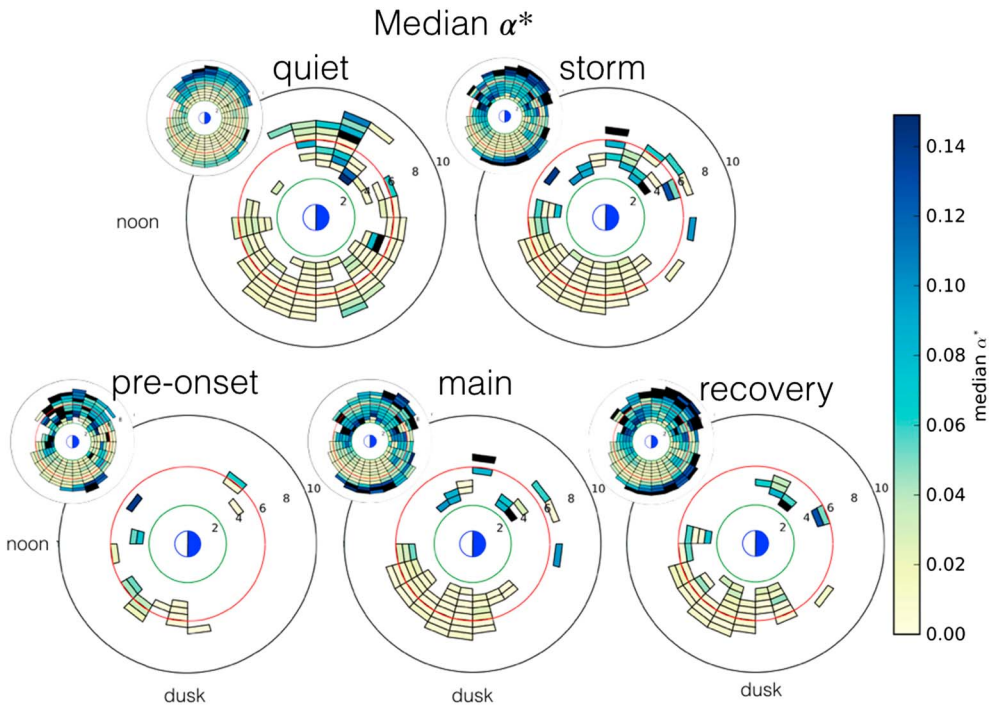

Figure 7. Polar plots of the median α^* during quiet, storm, preonset, main, and recovery phases. The inlaid polar plots show what the median α^* was in each bin for the times when EMIC waves were not observed for a geomagnetic condition. The green circle is at $L = 3$, the red at $L = 6$, and black at $L = 9$.

similar to quiet time values than those found during the main phase. The median, upper, and lower quartiles of α^* during EMIC waves are provided in the supporting information.

7. The Typical Wave Amplitude of EMIC Waves

Like α^*, the wave amplitude plays a large role in the calculation of the diffusion coefficients. The wave amplitude in part determines whether one can assume quasi-linear effects [e.g., *Summers*, 2005] or if one must take into account nonlinear effects [e.g., *Albert and Bortnik*, 2009]. Typical EMIC wave amplitudes tend to be much less than 1 nT with medians around 0.3 nT as shown in Figure 8, though peak wave amplitudes can be much higher [e.g., *Fraser et al.*, 2012]. Although there is some variation of the wave amplitudes observed between the different geomagnetic conditions, this parameter is relatively constant and is also the most evenly distributed. As this parameter is often cited to determine when one has to consider nonlinear dynamics, we have included polar plots of the upper and lower quartiles in Figures 9 and 10. Although the upper quartile in many bins does start to approach or exceed 1 nT, the majority of EMIC waves have amplitudes <1 nT. This has potentially large implications for modeling. Computing quasi-linear pitch angle diffusion coefficients is much less computationally expensive and, from the CRRES statistics, appears to often be a valid assumption.

8. Discussion/Conclusions

Although CRRES was unable to observe a large portion of the EMIC wave populations at $L > 7$ and in the noon sector due to its orbit and the mission concluding before it precessed through the noon sector, it was able to look closely at the region where EMIC waves may be a large contributor to storm time loss of the radiation belts. However, it is important to note that CRRES, like any individual satellite, is only able to sample at a single point location and a very small fraction of the magnetosphere during a geomagnetic storm and thus may not sample all EMIC waves for a given event. EMIC waves were observed during less than half of the CRRES era storms [*Halford et al.*, 2010; *Halford*, 2012]. Some of this may be due to the MLT of apogee, specifically when CRRES was primarily sampling the dawn and midnight sector during which approximately half the storms occurred it was unlikely to be sampling the region where EMIC waves typically occur. Although we try to remove the single point measurement bias by normalizing to the dwell time of the spacecraft in a given location bin, it is still possible that we are not able to compute accurate occurrence statistics given that

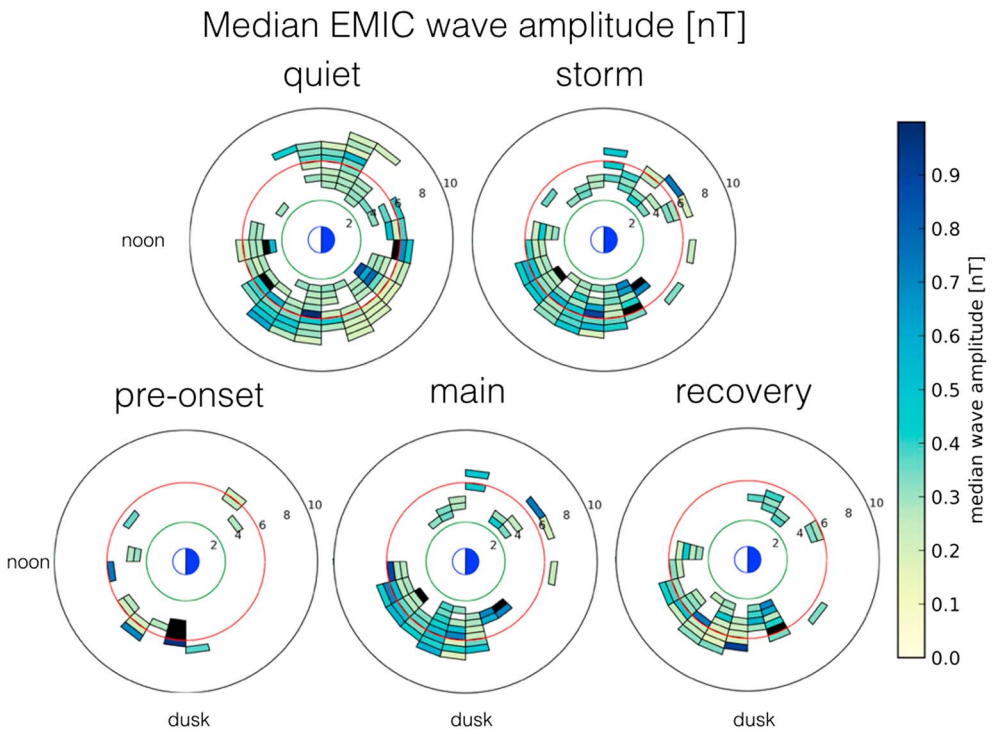

Figure 8. Polar plots of the median wave amplitude during quiet, storm, preonset, main, and recovery phases. The green circle is at $L = 3$, the red at $L = 6$, and black at $L = 9$.

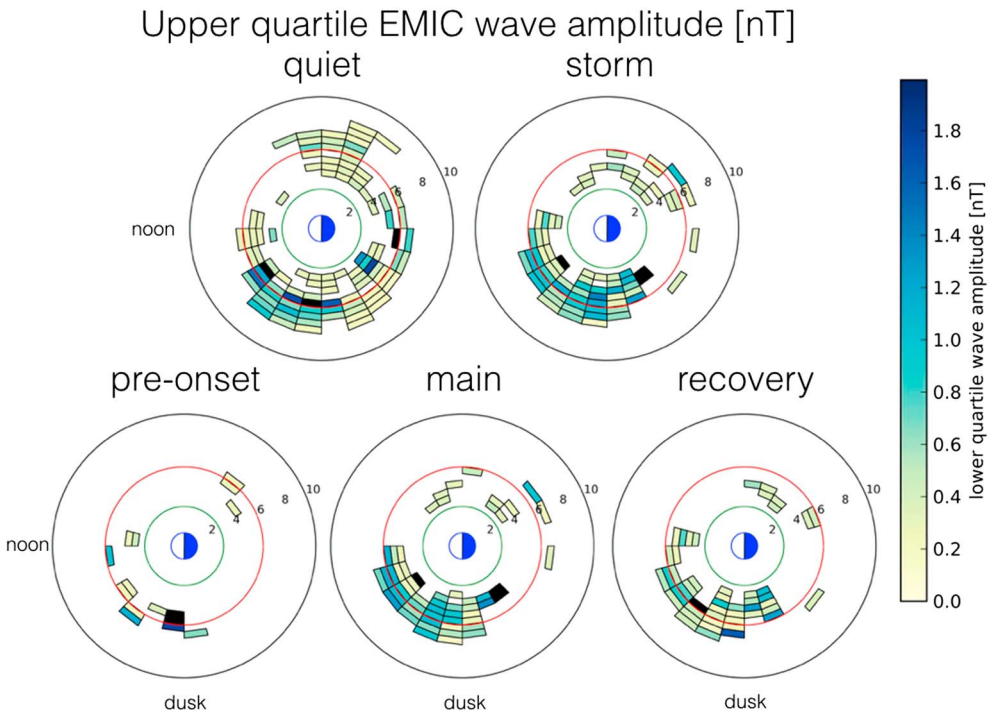

Figure 9. Polar plots of the upper quartile wave amplitude during quiet, storm, preonset, main, and recovery phases. The green circle is at $L = 3$, the red at $L = 6$, and black at $L = 9$.

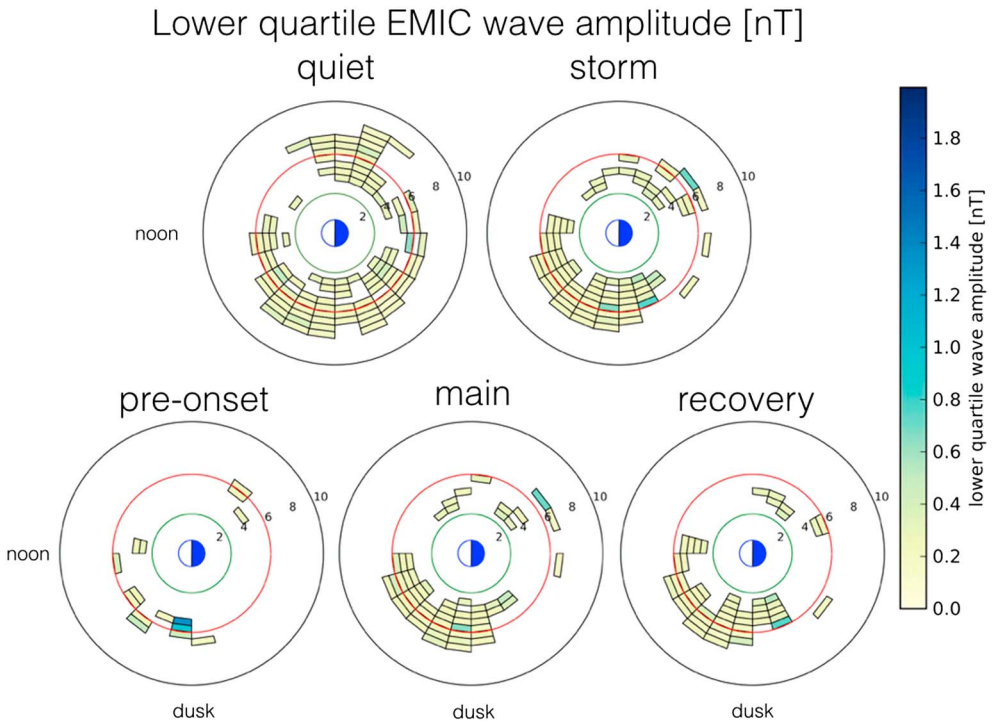

Figure 10. Polar plots of the lower quartile wave amplitude during quiet, storm, preonset, main, and recovery phases. The green circle is at $L = 3$, the red at $L = 6$, and black at $L = 9$.

we have less than a year's worth of data on the duskside where the majority of storm time EMIC waves are thought to occur and only took measurements during the declining phase of a very active solar cycle. However, as CRRES was operational during a very active solar cycle, these results may perhaps provide better storm time EMIC statistics than subsequent satellite missions which have been operational during the current very quiet solar maximum. Including observations from other missions in future studies, such as the Van Allen Probes, which have a similar orbit, will help determine the importance of the solar cycle activity, as well as provide increased statistics.

As we try to understand the relative importance of EMIC waves as well as other loss mechanisms to radiation belt dynamics, it is vital to determine when and where they occur and interact with radiation belt particles. We showed that this relationship is not well described by a single geomagnetic index, as the underlying physics is different between the phases of a geomagnetic storm. Although *Reeves et al.* [2003] have shown that the radiation belts respond inconsistently to geomagnetic storms, other studies have suggested that for both CME and CIR driven storms, there is consistently loss during the main phase [e.g., *Morley et al.*, 2010; *Murphy et al.*, 2015]. For all three indices, the main phase had either the highest occurrence rates and/or the broadest range of values with enhanced EMIC wave occurrence [e.g., *MacDonald et al.*, 2010]. Although we did not show that these waves are capable of pitch angle scattering radiation belt electrons into the atmosphere, this trend is suggestive that EMIC waves may be important to radiation belt dynamics specifically during the main phase of geomagnetic storms.

In summary and in addition to the results from *Halford et al.* [2010] and *Halford et al.* [2015], we find

1. The storm phase greatly changes the occurrence probability of EMIC waves for a given index value.
2. The median EMIC wave amplitude was found to be much less than 1 nT at ~0.3 nT.
3. EMIC waves occurring during the recovery phase saw plasma and wave characteristics closer to those found during geomagnetic quiet conditions than those observed during the main phase.

References

Albert, J. M., and J. Bortnik (2009), Nonlinear interaction of radiation belt electrons with electromagnetic ion cyclotron waves, *Geophys. Res. Lett.*, *36*, L12110, doi:10.1029/2009GL038904.

Allen, R. C., J. C. Zhang, L. M. Kistler, H. E. Spence, R. L. Lin, B. Klecker, M. W. Dunlop, M. André, and V. K. Jordanova (2015), A statistical study of EMIC waves observed by Cluster: 1. Wave properties, *J. Geophys. Res.*, *120*(7), 5574–5592.

Acknowledgments

This research was partly supported by Australian Research Council Project grant DP0772504 and Linkage International grant LX0882515. A.J. Halford was supported during her PhD by a University of Newcastle Postgraduate Research Scholarship and continued support by NASA under grant number NNX15AF66G. S.K.M. was supported by U.S. Department of Energy Laboratory Directed Research and Development (LDRD) award 20150127ER. S.E. was supported by NASA grant NNX14ACO4G and NNX15AF59G. A.A.C. was supported by NASA grant NNX15AI93G and NNX14AN55G. The *SYM-H*, *Kp*, and *AE* index were generated by the Kyoto data service whose construction of this database has been supported in part (as "Solar-Terrestrial Physics Database") by grants 127008, 168069, 178061, 188071, 198053, 208041, 218046, 228040, 238033, and 248032 under the Japan Society for Promotion of Science (JSPS) and can be found on the kyoto website http://wdc.kugi.kyoto-u.ac.jp/index.html. The event list used in this study is available on request from the corresponding author, A.J. Halford (alexa.j.halford@Dartmouth.edu). CRRES ephemeris and number density data are available on request from B.J. Fraser (brian.fraser@newcastle.edu.au). A.J.H. would like to thank Alex Glocer for useful discussions.

Anderson, B. J., R. E. Erlandson, and L. J. Zanetti (1992a), A statistical study of Pc 1-2 magnetic pulsations in the equatorial magnetosphere 1. Equatorial occurrence distributions, *J. Geophys. Res.*, *97*, 3075–3088.
Anderson, R. R., D. A. Gurnett, and D. L. Odem (1992b), CRRES plasma wave experiement, *J. Spacecr. Rockets*, *29*, 570–573.
Blum, L. W., E. A. Macdonald, S. P. Gary, M. F. Thomsen, and H. E. Spence (2009), Ion observations from geosynchronous orbit as a proxy for ion cyclotron wave growth during storm times, *J. Geophys. Res.*, *114*, A10214, doi:10.1029/2009JA014396.
Blum, L. W., et al. (2015), Observations of coincident EMIC wave activity and duskside energetic electron precipitation on 18–19 January 2013, *Geophys. Res. Lett.*, *42*, 5727–5735, doi:10.1002/2015GL065245.
Bossen, M., R. L. McPherron, and C. T. Russell (1976), A statistical study of Pc 1 magnetic pulsations at synchronous orbit, *J. Geophys. Res.*, *81*, 6083–6091.
Carter, B. A., E. Yizengaw, R. Pradipta, A. J. Halford, R. Norman, and K. Zhang (2015), Interplanetary shocks and the resulting geomagnetically induced currents at the equator, *Geophys. Res. Lett.*, *42*, 6554–6559, doi:10.1002/2015GL065060.
Cornwall, J. M. (1965), Cyclotron instabilities and electromagnetic emission in the ultra low frequency and very low frequency ranges, *J. Geophys. Res.*, *70*, 61–69.
Criswell, D. R. (1969), Pc 1 micropulsation activity and magnetospheric amplification of 0.2- to 5.0-Hz hydromagnetic waves, *J. Geophys. Res.*, *74*, 205–224, doi:10.1029/JA074i001p00205.
Denton, R. E., V. K. Jordanova, and B. J. Fraser (2014), Effect of spatial density variation and O+ concentration on the growth and evolution of electromagnetic ion cyclotron waves, *J. Geophys. Res. Space Physics*, *119*, 8372–8395, doi:10.1002/2014JA020384.
Denton, R. E., V. K. Jordanova, and J. Bortnik (2015), Resonance of relativistic electrons with electromagnetic ion cyclotron waves, *Geophys. Res. Lett.*, *42*, 8263–8270, doi:10.1002/2015GL064379.
Dessler, A. J., and E. N. Parker (1959), Hydromagnetic theory of geomagnetic storms, *J. Geophys. Res.*, *64*, 2239–2251.
Engebretson, M. J., M. R. Lessard, J. Bortnik, J. C. Green, R. B. Horne, D. L. Detrick, A. T. Weatherwax, J. Manninen, N. J. Petit, J. L. Posch, and M. C. Rose (2008), Pc1–Pc2 waves and energetic particle precipitation during and after magnetic storms: Superposed epoch analysis and case studies, *J. Geophys. Res.*, *113*, A01211, doi:10.1029/2007JA012362.
Fraser, B., S. Morley, R. Grew, and H. Singer (2012), Classification of Pc1-2 electromagnetic ion cyclotron waves at geosynchronous orbit, in *Dynamics of the Earth's Radiation Belts and Inner Magnetosphere*, edited by D. Summers et al., pp. 53–68, AGU, Washington, D. C.
Fraser, B. J., and T. S. Nguyen (2001), Is the plasmapause a preferred source region of electromagnetic cyclotron waves in the magnetosphere, *J. Atmos. Sol. Terr. Phys.*, *63*, 1225–1247.
Fraser, B. J., J. C. Samson, Y. D. Hu, R. L. McPherron, and C. T. Russell (1992), Electromagnetic ion cyclotron waves observed near the oxygen cyclotron frequency by ISEE 1 and 2, *J. Geophys. Res.*, *97*, 3063–3074, doi:10.1029/91JA02447.
Fraser, B. J., H. J. Singer, M. Adrian, and D. L. Gallagher (2005), The relationship between plasma density structure and EMIC waves at geosynchronous orbit, in *Geophysical Monograph*, vol. 159, edited by J. L. Burch, M. Schulz, and H. Spence, pp. 55–70, AGU, Washington, D. C.
Fraser, B. J., R. S. Grew, S. K. Morley, J. C. Green, H. J. Singer, T. M. Loto'aniu, and M. F. Thomsen (2010), Storm time observations of electromagnetic ion cyclotron waves at geosynchronous orbit: GOES results, *J. Geophys. Res.*, *115*, A05208, doi:10.1029/2009JA014516.
Friedel, R. H. W., S. Bourdarie, and T. E. Cayton (2005), Intercalibration of magnetospheric energetic electron data, *Space Weather*, *3*, S09B04, doi:10.1029/2005SW000153.
Gannon, J. L., X. Li, and D. Heynderickx (2007), Pitch angle distribution analysis of radiation belt electrons based on Combined Release and Radiation Effects Satellite Medium Electrons A data, *J. Geophys. Res.*, *112*, A05212, doi:10.1029/2005JA011565.
Gary, S. P., M. B. Moldwin, M. F. Thomsen, D. Winske, and D. J. Mccomas (1994), Hot proton anisotropies and cool proton temperatures in the outer magnetosphere, *J. Geophys. Res.*, *99*, 23,603–23,615, doi:10.1029/94JA02069.
Gerrard, A., L. Lanzerotti, M. Gkioulidou, D. Mitchell, J. Manweiler, J. Bortnik, and K. Keika (2014), Initial measurements of O-ion and He-ion decay rates observed from the Van Allen probes RBSPICE instrument, *J. Geophys. Res. Space Physics*, *119*, 8813–8819, doi:10.1002/2014JA020374.
Glocer, A., G. Tóth, T. Gombosi, and D. Welling (2009), Modeling ionospheric outflows and their impact on the magnetosphere, initial results, *J. Geophys. Res.*, *114*, A05216, doi:10.1029/2009JA014053.
Gomberoff, L., and R. Neira (1983), Convective growth rate of ion cyclotron waves in a H^+-He^+ and H^+-He^+-O^+ plasma, *J. Geophys. Res.*, *88*, 2170–2174, doi:10.1029/JA088iA03p02170.
Halford, A. J. (2012), EMIC wave association with geomagnetic storms, the plasmasphere, and the radiation belts, PhD thesis, Callaghan NSW Australia.
Halford, A. J., B. J. Fraser, and S. K. Morley (2010), EMIC wave activity during geomagnetic storm and nonstorm periods: CRRES results, *J. Geophys. Res.*, *115*, A12248, doi:10.1029/2010JA015716.
Halford, A. J., B. J. Fraser, and S. K. Morley (2015), EMIC waves and plasmaspheric and plume density: CRRES results, *J. Geophys. Res. Space Physics*, *120*, 1974–1992, doi:10.1002/2014JA020338.
Horne, R. B., T. Kersten, S. A. Glauert, N. P. Meredith, D. Boscher, A. Sicard-Piet, R. M. Thorne, and W. Li (2013), A new diffusion matrix for whistler mode chorus waves, *J. Geophys. Res. Space Physics*, *118*, 6302–6318, doi:10.1002/jgra.50594.
Ilie, R., M. W. Liemohn, M. F. Thomsen, J. E. Borovsky, and J. Zhang (2008), Influence of epoch time selection on the results of superposed epoch analysis using ACE and MPA data, *J. Geophys. Res.*, *113*, A00A14, doi:10.1029/2008JA013241.
Ishida, J., S. Kokubun, and R. L. McPherron (1987), Substorm effects on spectral structures of Pc 1 waves at synchronous orbit, *J. Geophys. Res.*, *92*, 143–158.
Jordanova, V. K. (2007), Modeling geomagnetic storm dynamics: New results and challenges, *J. Atmos. Terr. Phys.*, *69*, 56–66, doi:10.1016/j.jastp.2006.06.016.
Kamide, Y., and S.-I. Akasofu (1983), Notes on the auroral electrojet indices, *Rev. Geophys.*, *21*, 1647–1656.
Kangas, J., A. Guglielmi, and O. Pokhotelov (1998), Morphology and physics of short-period magnetic pulsations, *Space Sci. Rev.*, *83*, 435–512.
Kasahara, Y., A. Sawada, M. Yamamoto, I. Kimura, S. Kokubun, and K. Hayashi (1992), Ion cyclotron emissions observed by the satellite Akebono in the vicinity of the magnetic equator, *Radio Sci.*, *27*(2), 347–362.
Katus, R. M., M. W. Liemohn, E. L. Ionides, R. Ilie, D. Welling, and L. K. Sarno Smith (2015), Statistical analysis of the geomagnetic response to different solar wind drivers and the dependence on storm intensity, *J. Geophys. Res. Space Physics*, *120*, 310–327, doi:10.1002/2014JA020712.
Keika, K. (2013), Global characteristics of electromagnetic ion cyclotron waves: Occurrence rate and its storm dependence, *J. Geophys. Res. Space Physics*, *118*, 4135–4150, doi:10.1002/jgra.50385.
Kim, E. H., and J. R. Johnson (2016), Full-wave modeling of EMIC waves near the He+ gyrofrequency, *Geophys. Res. Lett.*, *43*, 13–21, doi:10.1002/2015GL066978.

Kotova, G. A. (2007), The Earth's plasmasphere: State of studies (A review), *Geomagn. Aeron.*, *47*, 409–422, doi:10.1134/S0016793207040019.
Kozyra, J. U., T. E. Cravens, A. F. Nagy, E. G. Fontheim, and R. S. B. Ong (1984), Effects of energetic heavy ions on electromagnetic ion cyclotron wave generation in the plasmapause region, *J. Geophys. Res.*, *89*, 2217–2233.
Li, W., R. Thorne, V. Angelopoulos, J. Bortnik, C. M. Cully, B. Ni, O. LeContel, A. Roux, U. Auster, and W. Magnes (2009), Global distribution of whistler-mode chorus waves observed on the THEMIS spacecraft, *Geophys. Res. Lett.*, *36*, L09104, doi:10.1029/2009GL037595.
Liu, Y., B. Fraser, and F. Menk (2012), Pc2 EMIC waves generated high off the equator in the dayside outer magnetosphere, *Geophys. Res. Lett.*, *39*, L17102, doi:10.1029/2012GL053082.
Liu, Y., B. Fraser, F. Menk, J.-C. Zhang, L. Kistler, and I. Dandouras (2013), Correction to "Pc2 EMIC waves generated high off the equator in the dayside outer magnetosphere", *Geophys. Res. Lett.*, *40*, 1950–1951, doi:10.1002/grl.50283.
MacDonald, E. A., L. W. Blum, S. P. Gary, M. F. Thomsen, and M. H. Denton (2010), High-speed stream driven inferences of global wave distributions at geosynchronous orbit: Relevance to radiation-belt dynamics, *Proc. R. Soc. A*, *466*(2123), 3351–3362, doi:10.1098/rspa.2010.0076.
McCollough, J. P., S. R. Elkington, M. E. Usanova, I. R. Mann, D. N. Baker, and Z. C. Kale (2010), Physical mechanisms of compressional EMIC wave growth, *J. Geophys. Res.*, *115*, A10214, doi:10.1029/2010JA015393.
McCollough, J. P., S. R. Elkington, and D. N. Baker (2012), The role of Shabansky orbits in compression-related electromagnetic ion cyclotron wave growth, *J. Geophys. Res.*, *117*, A01208, doi:10.1029/2011JA016948.
McIlwain, C. (1966), Magnetic coordinates, *Space Sci. Rev.*, *5*, 585–598.
Meredith, N., R. Thorne, R. Horne, D. Summers, B. Fraser, and R. Anderson (2003), Statistical analysis of relativistic electron energies for cyclotron resonance with EMIC waves observed on CRRES, *J. Geophys. Res.*, *108*(A6), 1250, doi:10.1029/2002JA009700.
Meredith, N. P., R. B. Horne, T. Kersten, B. J. Fraser, and R. S. Grew (2014), Global morphology and spectral properties of EMIC waves derived from CRRES observations, *J. Geophys. Res. Space Physics*, *119*, 5328–5342, doi:10.1002/2014JA020064.
Min, K., J. Lee, K. Keika, and W. Li (2012), Global distribution of EMIC waves derived from THEMIS observations, *J. Geophys. Res.*, *117*, A05219, doi:10.1029/2012JA017515.
Morley, S., M. G. Henderson, G. D. Reeves, R. H. W. Friedel, and D. N. Baker (2013), Phase space density matching of relativistic electrons using the Van Allen Probes: REPT results, *Geophys. Res. Lett.*, *40*, 4798–4802, doi:10.1002/grl.50909.
Morley, S. K., R. H. W. Friedel, E. L. Spanswick, G. D. Reeves, J. T. Steinberg, J. Koller, T. Cayton, and E. Noveroske (2010), Dropouts of the outer electron radiation belt in response to solar wind stream interfaces: Global positioning system observations, *Proc. R. Soc. A*, *466*, 3329–3350, doi:10.1098/rspa.2010.0078.
Morley, S. K., J. P. Sullivan, M. G. Henderson, J. B. Blake, and D. N. Baker (2016), The Global Positioning System constellation as a space weather monitor: Comparison of electron measurements with Van Allen Probes data, *Space Weather*, *14*, 76–92, doi:10.1002/2015SW001339.
Murphy, K. R., I. R. Mann, and D. G. Sibeck (2015), On the dependence of storm-time ULF wave power on magnetopause location: Impacts for ULF wave radial diffusion, *Geophys. Res. Lett.*, *42*, 9676–9684, doi:10.1002/2015GL066592.
Ni, B., Y. Shprits, T. Nagai, R. Thorne, Y. Chen, D. Kondrashov, and H.-j. Kim (2009), Reanalyses of the radiation belt electron phase space density using nearly equatorial CRRES and polar-orbiting Akebono satellite observations, *J. Geophys. Res.*, *114*, A05208, doi:10.1029/2008JA013933.
Olson, J. V., and L. C. Lee (1983), Pc1 wave generation by sudden impulses, *Planet. Space Sci.*, *31*, 295–302, doi:10.1016/0032-0633(83)90079-X.
Olson, W. P., and K. A. Pfitzer (1974), A quantitative model of the magnetospheric magnetic field, *J. Geophys. Res.*, *79*, 3739–3748, doi:10.1029/JA079i025p03739.
Omidi, N., J. Bortnik, R. Thorne, and L. Chen (2013), Impact of cold O^+ ions on the generation and evolution of EMIC waves, *J. Geophys. Res. Space Physics*, *118*, 434–445, doi:10.1029/2012JA018319.
Reeves, G. D., K. L. McAdams, R. H. W. Friedel, and T. P. O'Brien (2003), Acceleration and loss of relativistic electrons during geomagnetic storms, *Geophys. Res. Lett.*, *30*(10), 1529, doi:10.1029/2002GL016513.
Rostoker, G. (1972), Geomagnetic indices, *Rev. Geophys.*, *10*(4), 935–950.
Saba, M. F., W. Gonzalez, and A. Clúa de Gonzalez (1997), Relationships between the AE, ap and Dst indices near solar minimum (1974) and at solar maximum (1979), *Ann. Geophys.*, *15*(10), 1265–1270.
Saikin, A., J.-C. Zhang, R. Allen, C. Smith, L. Kistler, H. Spence, R. Torbert, C. Kletzing, and V. K. Jordanova (2015), The occurrence and wave properties of H^+-, HE^+-, and O^+-band EMIC waves observed by the Van Allen Probes, *J. Geophys. Res. Space Physics*, *120*, 7477–7492, doi:10.1002/2015JA021358.
Sandanger, M. I., F. Søraas, M. Sørbø, K. Aarsnes, K. Oksavik, and D. S. Evans (2009), Relativistic electron losses related to EMIC waves during CIR and CME storms, *J. Atmos. Sol. Terr. Phys.*, *71*(10-11), 1126–1144, doi:10.1016/j.jastp.2008.07.006.
Sckopke, N. (1966), A general relation between the energy of trapped particles and the disturbance field near the Earth, *J. Geophys. Res.*, *71*, 3125–3130.
Shprits, Y., D. Kondrashov, Y. Chen, R. Thorne, M. Ghil, R. Friedel, and G. Reeves (2007), Reanalysis of relativistic radiation belt electron fluxes using CRRES satellite data, a radial diffusion model, and a Kalman filter, *J. Geophys. Res.*, *112*, A12216, doi:10.1029/2007JA012579.
Shprits, Y., A. Kellerman, D. Kondrashov, and D. Subbotin (2013), Application of a new data operator-splitting data assimilation technique to the 3-D VERB diffusion code and CRRES measurements, *Geophys. Res. Lett.*, *40*, 4998–5002, doi:10.1002/grl.50969.
Singer, H. J., W. P. Sullivan, P. Anderson, F. Mozer, P. Harvey, J. Wygant, and W. William (1992), Fluxgate magnetometer instrument on the CRRES, *J. Spacecr. Rockets*, *29*, 599–601.
Siscoe, G. L., and N. U. Crooker (1974), On the partial ring current contribution to Dst, *J. Geophys. Res.*, *79*, 1110–1112.
Spasojevic, M., and S. A. Fuselier (2009), Temporal evolution of proton precipitation associated with the plasmaspheric plume, *J. Geophys. Res.*, *114*, A12201, doi:10.1029/2009JA014530.
Spasojevic, M., J. Goldstein, D. L. Carpenter, U. S. Inan, B. R. Sandel, M. B. Moldwin, and B. W. Reinisch (2003), Global response of the plasmasphere to a geomagnetic disturbance, *J. Geophys. Res.*, *108*, 1340, doi:10.1029/2003JA009987.
Sugiura, M. (1964), Hourly values of equatorial Dst for the IGY, *Ann. Int. Geophys. Year*, *9*, 9–45.
Summers, D. (2005), Quasi-linear diffusion coefficients for field-aligned electromagnetic waves with applications to the magnetosphere, *J. Geophys. Res.*, *110*, A08213, doi:10.1029/2005JA011159.
Summers, D., and R. Thorne (2003), Relativistic electron pitch-angle scattering by electromagnetic ion cyclotron waves during geomagnetic storms, *J. Geophys. Res.*, *108*(A4), 1143, doi:10.1029/2002JA009489.
Summers, D., B. Ni, and N. Meredith (2007a), Timescales for radiation belt electron acceleration and loss due to resonate wave-particle interactions: 2. evaluation for VLF chorus, ELF hiss, and electromagnetic ion cyclotron waves, *J. Geophys. Res.*, *112*, A04207, doi:10.1029/2006JA011993.

Summers, D., B. Ni, and N. P. Meredith (2007b), Timescales for radiation belt electron acceleration and loss due to resonant wave-particle interactions: 1. Theory, *J. Geophys. Res.*, *112*, A04206, doi:10.1029/2006JA011801.

Thomsen, M. F. (2004), Why *Kp* is such a good measure of magnetospheric convection, *Space Weather*, *2*, S11004, doi:10.1029/2004SW000089.

Tsyganenko, N. A., and M. I. Sitnov (2005), Modeling the dynamics of the inner magnetosphere during strong geomagnetic storms, *J. Geophys. Res.*, *110*, A03208, doi:10.1029/2004JA010798.

Usanova, M. E., I. R. Mann, J. Bortnik, L. Shao, and V. Angelopoulos (2012), THEMIS observations of electromagnetic ion cyclotron wave occurrence: Dependence on AE, SYMH, and solar wind dynamic pressure, *J. Geophys. Res.*, *117*, A10218, doi:10.1029/2012JA018049.

Usanova, M. E., F. Darrouzet, I. R. Mann, and J. Bortnik (2013), Statistical analysis of EMIC waves in plasmaspheric plumes from Cluster observations, *J. Geophys. Res. Space Physics*, *118*, 4946–4951, doi:10.1002/jgra.50464.

Usanova, M. E., et al. (2014), Effect of EMIC waves on relativistic and ultrarelativistic electron populations: Ground based and van allen probes observations, *Geophys. Res. Lett*, *41*, 1375–1381, doi:10.1002/2013GL059024.

Wanliss, J. A., and K. M. Showalter (2006), High-resolution global storm index: Dst versus Sym-H, *J. Geophys. Res.*, *111*, A02202, doi:10.1029/2005JA011034.